

# Discharge Plasma Parameters of a 30-cm Ion Thruster Measured without Beam Extraction using a High-Speed Probe Positioning System\*

Daniel A. Herman<sup>†</sup>, Daniel S. McFarlane<sup>‡</sup>, and Alec D. Gallimore<sup>§</sup>  
Plasmadynamics and Electric Propulsion Laboratory  
University of Michigan  
Ann Arbor, MI 48105 USA

## Abstract

A method for delivering a symmetric double probe into the discharge chamber of a 30-cm diameter ring-cusped ion thruster is demonstrated. Motivation for direct access of the electrostatic probe to the discharge chamber stems from the need to characterize the discharge plasma to better understand the possible cause of discharge cathode assembly (DCA) erosion. A symmetric double probe allows electron temperature and number density measurements with minimal perturbation to the discharge plasma and thruster operation. The High-speed Axial Reciprocating Probe positioning system (HARP) was used to further minimize thruster perturbation during probe insertion. Internal mechanism problems restricted previous double probe measurements to one axial location. A new, slightly modified setup allowed a complete two-dimensional mapping of the discharge plasma parameters at one thruster operating condition *without beam extraction*. The electron number density was found to range from  $1 \times 10^{10} - 2 \times 10^{12} \text{ cm}^{-3}$  inside the discharge chamber with the maximum occurring at DCA centerline, which is consistent with other results. Electron temperature ranged from 2 – 3.3 eV, which is consistent with predictions for ion thrusters incorporating a ring-cusped design. The appearance of an off-axis maximum in electron temperature necessitates further testing to confirm and explain.

## Nomenclature

$A_p$	Probe surface area, $\text{m}^2$	$P_c$	Corrected pressure (on xenon), Torr
$A_s$	Ion Collection Area, $\text{m}^2$	$R_{eq}$	Equivalent Resistance, $\Omega$
$e$	Electron charge, $1.6 \times 10^{-19} \text{ C}$	$R_p$	Probe Electrode Radius, m
$i$	collected current, mA	$R_{plasma}$	Plasma Resistance, $\Omega$
$i_{ion,sat}$	Ion saturation current, A	$T_e$	Electron temperature, eV
$I_a$	Acceleration grid current, mA	$V_{Batteries}$	Battery Bias Voltage, V
$I_b$	Beam current, A	$V_{ck-cc}$	Cathode Keeper floating potential with respect to Cathode Common
$I_d$	Discharge current, A	$V_d$	Discharge voltage, V
$I_{nk}$	Neutralizer keeper current, A	$V_g$	Neutralizer to ground coupling voltage, V
$k$	Boltzmann's constant, $1.38 \times 10^{-23} \text{ J/K}$	$V_s$	Screen grid voltage, V
$M_{Xe}$	Atomic mass of xenon, kg	$V_a$	Acceleration grid voltage, V
$n_e$	Electron number density, $\text{m}^{-3}$	$V_{nk}$	Neutralizer keeper voltage, V
$P_b$	Base pressure (air), Torr	$\phi$	Probe bias potential, V
$P_i$	Indicated pressure (with xenon flow), Torr		

\* Presented as Paper IEPC-03-0069 at the 28<sup>th</sup> International Electric Propulsion Conference, Toulouse, France, March 17 – 21, 2003. Published by the Electric Rocket Propulsion Society with permission.

<sup>†</sup> Graduate Student, Aerospace Engineering, hermo@engin.umich.edu.

<sup>‡</sup> Graduate Student, Aerospace Engineering.

<sup>§</sup> Associate Professor and Laboratory Director.

## Introduction

Ion thrusters are high efficiency, high specific impulse ( $I_{sp}$ ) propulsion systems that have been proposed as the primary propulsion source for a variety of missions. The NASA Solar Electric Propulsion Technology Applications Readiness (NSTAR) 30 cm ion thruster was the first ion engine to be used for primary propulsion and has demonstrated operation for over three times its intended lifetime.<sup>1</sup> Although this places NSTAR as the record holder for the most hours of operation for an in-space thruster, efforts to further increase engine lifetime continue.

A potential failure mechanism for ion engine technology is erosion of the Discharge Cathode Assembly's (DCA) downstream surface.<sup>2</sup> In order to mitigate DCA erosion on NSTAR, an engineering solution of adding a cathode keeper electrode was employed.<sup>3</sup> This led to a decrease in DCA erosion and, until recently, was thought to have solved the DCA erosion issue. An ongoing Extended Life Test (ELT) of the flight spare thruster is being conducted at the Jet Propulsion Laboratory (JPL).<sup>4</sup> Extensive discharge cathode keeper erosion has been observed after 12,000 hours of testing, which has yet to be fully explained.<sup>5</sup>

Laser-Induced Fluorescence (LIF) measurements done by Williams<sup>6</sup> have suggested the existence of a potential hill downstream of the DCA as a possible cause of DCA erosion. Mapping of the internal plasma structure of the ion engine, specifically downstream of the DCA, is essential to understanding the cause of discharge cathode erosion. Direct measurement of plasma properties such as electron temperature, electron number density, and plasma potential would permit evaluation of the sensitivity of the discharge parameters on operating condition. Characterizing the dependence of the discharge plasma on operating condition would aid in determining the cause of DCA erosion and how to minimize it. The intention of this paper is to demonstrate a method for mapping electron number density and electron temperature inside the discharge chamber of an ion thruster.

## 30 cm Ion Thruster

### Background

The Functional Model Thruster (FMT) preceded the NSTAR Engineering Model Thruster (EMT) and the NSTAR Flight Thruster. The principal

difference in the construction of the FMT from the EMT was the anode material. The FMT anode was aluminum while the EMT anode was spun aluminum and titanium. The second of two FMTs, FMT-2, was modified at the NASA Glenn Research Center (GRC) by Williams to allow optical access to the discharge chamber for the purpose of LIF measurements.<sup>6</sup> Six slots were cut into FMT-2: three slots in the plasma shield and three slots in the anode.

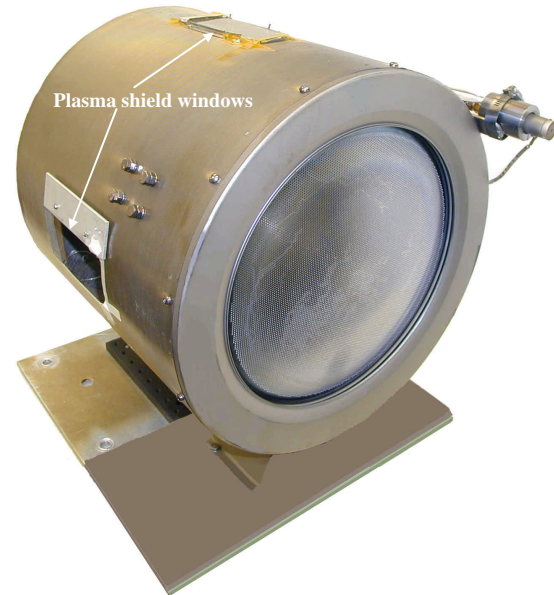


Fig. 1 – Photograph of the FMT-2 ion thruster indicating side and top plasma shield windows (bottom window not shown).

Three quartz windows covered the rectangular slots cut into the FMT-2 anode wall. These three slots, each 10.2 cm by 3.2 cm, replaced roughly twenty percent of the anode surface.<sup>6</sup> The side slots of the plasma shield and anode are shown in Fig. 2.

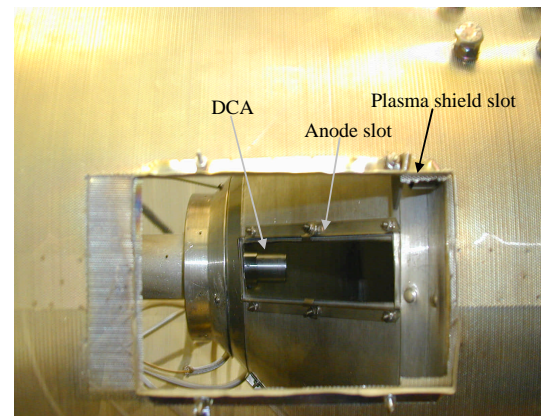


Fig. 2 – Side LIF slots and window mounts with windows removed.

The magnetic field, DCA, and geometry of the discharge chamber were identical to EMT-1's.<sup>6</sup> For a more complete comparison between FMT-2 and EMT-1 see Reference 6. The thruster has been operated over the entire NSTAR power throttling range at GRC and at the Plasmadynamics and Electric Propulsion Laboratory (PEPL) illustrating comparable performance to the EMTs and flight thrusters. Williams has shown that these modifications have not altered the engine's magnetic field, discharge chamber performance, or thruster performance.<sup>6</sup>

### New FMT-2 Modifications

To allow an electrostatic probe access inside the anode, two of the existing windows and their mounts, one in the plasma shield side and the other in the anode side, were removed. The top and bottom windows of both the plasma shield and the anode were not altered. The criteria for selection of modifications was based on the following requirements: minimal thruster alterations, access into the discharge chamber for the probe, automated axial movement of the electrostatic probe, complete enclosure of the existing slot in the anode to contain the discharge plasma, and elimination of the line of sight from outside the plasma shield to the anode.

The design selected, shown in Figs. 3, 4, and 5, was installed in FMT-2. By retracting as the probe is moved downstream of the DCA, and extending when moved towards the DCA, the translating dielectric tube minimized the protrusion of material into the discharge chamber. The 44-gauge, stainless steel, plasma containment sheet pressed flush against the anode by two sets of guides. The inner guides (closest to the anode) were given a curl at the downstream end in order to reduce the risk of crimping the thin stainless foil when the probe moved in the axial direction. Non-magnetic stainless steel hardware preserved the magnetic field topography. The 99.8% pure alumina translating tube was machined with an angle to further reduce protrusion into the discharge chamber. The tube was mounted onto a small New England Affiliated Technologies (NEAT) RMS-800 single axis ball screw table controlled via computer. The table has a lead screw accuracy of 80  $\mu\text{m}$ . Fiberglass tape minimized electric fields at the sharp edges of the containment sheet. A rectangular piece of Macor was mounted on the inside surface of the plasma shield to avoid contact of the curling guide with the plasma shield.

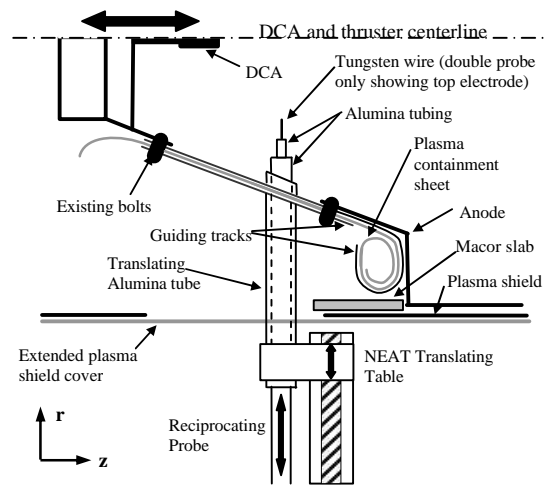


Fig. 3 – Modified FMT-2 schematic (horizontal cross section).

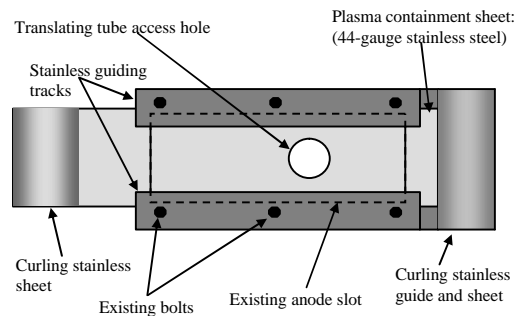


Fig. 4 – Modified FMT-2 schematic showing the side view of the hardware covering the anode side slot.

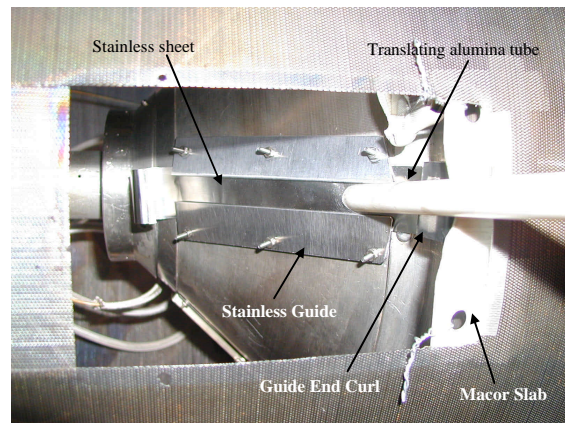


Fig. 5 – Picture of internal mechanism showing discharge plasma containment looking through plasma shield slot (Plasma shield cover removed).

## Apparatus and Procedure

### Vacuum Facility

All experiments were performed in the 6 m by 9 m Large Vacuum Test Facility (LVTF) at PEPL. Four CVI Model TM-1200 Re-Entrant Cryopumps provided a combined pumping speed of 140,000 l/s on xenon with a base pressure of  $2.5 \times 10^{-7}$  Torr. Chamber pressure was recorded using two hot-cathode ionization gauges. The pressure reported is an average of the two corrected readings. A complete neutral pressure map of the LVTF has shown that the average pressure is a conservative measure of the tank pressure in this facility.<sup>7</sup> Pressure measurements from each gauge were corrected for xenon using the known base pressure on air and a correction factor of 2.87 for xenon according to,<sup>8,9</sup>

$$P_c = \frac{P_i - P_b}{2.87} + P_b. \quad (1)$$

A dedicated propellant feed system, consisting of three Edwards mass flow controllers, provided by NASA GRC, controlled the xenon flow to the thruster. The flow rates were calibrated over their entire operating range using a known volume technique prior to operation. Another flow rate calibration was done post test.

A 2 m by 2.5 m louvered graphite panel beam dump was positioned approximately 4 m downstream of the FMT-2 during operation to reduce back sputtering. The thruster was operated at PEPL using a modified Skit-Pac provided by NASA GRC.

### Axial Movement

The FMT-2 was mounted on a custom built, two-axis positioning system consisting of two NEAT translational stages. The upper axis was used to maintain a constant radial distance between the thruster and the High-speed Axial Reciprocating Probe (HARP) positioning system. The lower axis controlled the engine axial location with respect to the probe to an absolute position accuracy of 0.15 mm. The electrostatic probe was radially positioned inside the discharge chamber using the HARP. The HARP system was fixed with respect to the chamber. When actuated, the probe extended to the thruster centerline then returned to the starting location just inside the translating alumina tube. The small RMS-800 NEAT table retracted and extended the translating alumina tube as the axial location changed. The

end of the tube was stationed 5 mm inside the discharge chamber at all times, thus minimally perturbing the discharge plasma.

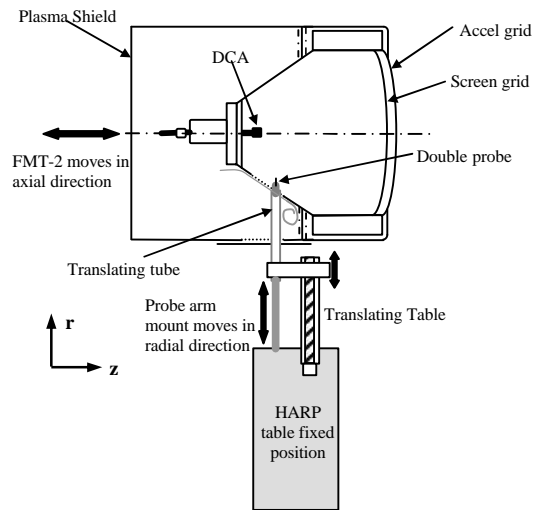


Fig. 6 – Schematic of FMT-2 orientation with respect to the HARP for probe insertion.

### High-speed Axial Reciprocating Probe (HARP)

A linear motor assembly provided highly accurate direct linear motion of the probe with minimal residence times. The HARP system is a three-phase brushless dc servo motor consisting of a linear “U”-shaped magnet track and a “T”-shaped coil moving on a set of linear tracks. The linear encoder provided positioning resolution to 5  $\mu\text{m}$ .<sup>10</sup> A Pacific Scientific SC950 digital, brushless servo drive was used to control the motor. A PC monitored and controlled the servo drive via serial cable. The entire table was enclosed in a stainless steel shroud with a graphite outer skin. A probe boom mounted on the table platform facilitated probe mounting and replacement. Residence times of the probe inside the discharge chamber were kept under one second to minimize probe heating and discharge plasma perturbation.

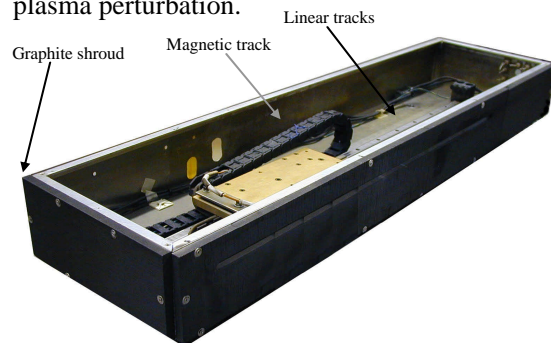


Fig. 7 – High-speed Axial Reciprocating Probe (HARP) positioning table with top cover removed (probe not installed).

## Electrostatic Probe

### Probe Type

Probes always perturb their surroundings; the extent of the perturbation is minimized by physically making the probe as small as possible. This bodes well with the need to maintain spatial resolution when making measurements. To minimize the plasma losses to the probe, the probe size was minimized while maintaining a measurable current from the predicted plasma parameters.

Several factors were taken into consideration when designing the electrostatic probe, the first being the type of probe. Unlike the single Langmuir probe, the double probe floats as a whole and thus causes less perturbation to the discharge plasma environment.<sup>11</sup> The symmetric geometry about the discharge cathode orifice made using a triple probe less attractive. A symmetric double probe was selected because the simplicity in data analysis outweighed the benefits gained by sampling more of the electron energy distribution, accomplished using an asymmetric double probe.

### Double Probe Hardware

The electrodes of the double probe were sized such that, for the expected electron temperature ( $2 - 11$  eV)<sup>12, 13</sup> and number densities ( $1 \times 10^{10} - 1 \times 10^{12}$  cm<sup>-3</sup>),<sup>12, 14</sup> the probe operates in the thin sheath regime. The number densities are expected to vary over two orders of magnitude driving and ever increasing Debye length. The rapid growth in the Debye length dictates that, at some radial location inside the anode, the thin sheath criterion will not strictly apply. The thin sheath calculation will still be used until the Debye length is on the order of the electrode radius as the expansion of the collection area with increasing Debye length is accounted for in the data analysis. Probe sheaths are often assumed approximately equal to the Debye length as is done in our analysis though this can underestimate sheath thickness for large negative electrode bias.<sup>15</sup> In the thin sheath regime, the flux of particles entering the sheath can be calculated without considering the details about the orbits of these particles in the sheath. In this case, the collection area of the electrode is initially approximated as the area of the electrode. This approximation is justified for a large ratio of probe radius to Debye length,  $\lambda_D$ .<sup>11, 15, 16</sup>

A large length to diameter ratio minimized end effects. A conservative gap distance, distance between the electrodes, maintained at least ten Debye lengths between electrodes to avoid overlapping of electrode sheaths. The size of the electrodes was chosen so that the current collected by the probe is large enough to be measured accurately, but much smaller than the discharge current to avoid unduly perturbing the discharge plasma.

The double probe used, shown in Fig. 8, consisted of two 0.24 mm diameter cylindrical tungsten electrodes with 5.1 mm exposed length. The electrodes are held inside two double bore pieces of alumina epoxied to one larger double bore piece of alumina. The alumina was covered with a floating stainless steel tube to shield the tungsten wires. The total length of the tungsten and alumina was approximately 46 cm (18 inches) with 4.4 cm of alumina left unshielded towards the exposed end. The “double tier” design reduces the amount of blockage mass that is inserted into the discharge cathode plume. This new design eliminated the visual perturbation originally seen during insertion to the discharge plasma.

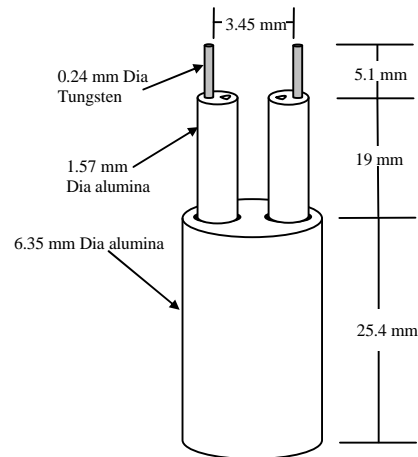


Fig. 8 – Schematic of the new reduced blockage double probe design showing the exposed alumina end.

### Double Probe Electronics

As the probe is inserted into the discharge chamber, the floating potential can reach 1100 V, causing difficulty for most electronics. Significant errors in the measured current can occur due to any appreciable stray capacitance in the circuit. Careful attention to the circuit design minimized stray capacitance and batteries were used to supply the bias voltage.<sup>17</sup> The battery

supply consisted of two series groups of four 67.5-volt zinc-manganese dioxide batteries connected in parallel. The batteries were capable of outputting 135 V at 100 mA. A potentiometer was attached to the battery output to adjust the electrode bias voltage.

The double probe circuit had been used previously to make similar measurements inside the discharge channel of a Hall Thruster.<sup>17</sup> The double probe circuit was built around two Analog Devices AD210 isolation amplifiers. These amplifiers are capable of handling up to 2500 volts of common mode voltage and provide an input impedance of  $1 \times 10^{12} \Omega$ . The low impedance output ( $1 \Omega$  maximum) was connected to a digital oscilloscope that, when triggered off the probe position, recorded the data and saved it to a computer. Figure 9 illustrates the double probe circuit.

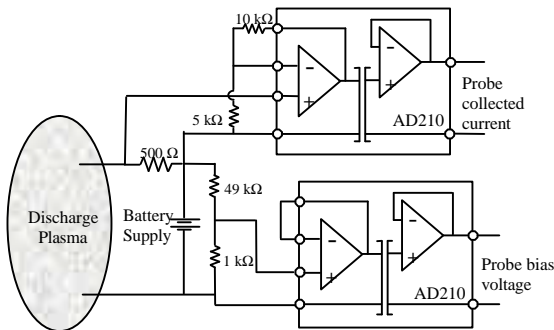


Fig. 9 – Double probe circuit electrical diagram.

The outputs of the isolation amplifiers were calibrated with known currents and bias voltages over their entire operating ranges. A digital source meter was connected across the two electrodes to simulate the collected current of the probe. The output of the probe current shunt was then measured as a function of known supplied current, resulting in a linear calibration curve. A similar calibration of the bias voltage output was done by applying known bias voltages between the electrodes and measuring the probe bias voltage output from the circuit.

### Data Acquisition

To reduce data collection time, all three NEAT tables were controlled by one LabVIEW code that allowed multiple input positions, the ability to wait at a given location, the ability to trigger the HARP, and finally record the data from the oscilloscope after each sweep. This automation translated into increased resolution for a given amount of time.

The two NEAT translational stages and small NEAT RMS-800 stage were controlled via GPIB connections. The LabVIEW code stepped through the full axial range of motion (approximately 4 cm) in 1.5875 mm increments. For each step, the program retracted the alumina translating tube, swept the HARP, and dwelled for the amount of time required for HARP sweep. After all axial locations were interrogated, the computer returned the FMT-2 to the zero position located 2 mm downstream of the DCA exit plane. Bias voltages were set manually using a potentiometer and the battery supply.

The HARP was controlled by a separate computer using serial connections. An oscilloscope triggered off of the HARP position and recorded all data. The oscilloscope recorded probe position, probe collected current, probe bias voltage, and the discharge current (from a Hall sensor) as a function of time during probe insertion.

### Reduction of Bias Voltage Sag

Prior testing exposed a noticeable drop in the bias voltage observed during probe insertion. It is desirable to minimize this if possible. However, it is important to note that even if a noticeable bias voltage “sag” occurs the double probe circuit, measuring the bias voltage as a function of position, can take this “sag” into account during data analysis.

Zinc-manganese dioxide instrument batteries supplied the probe bias voltage. Figure 10 shows that the voltage sag is roughly 2% of the set bias voltage for this case. The voltage drop magnitude decreased for lower bias voltage settings.

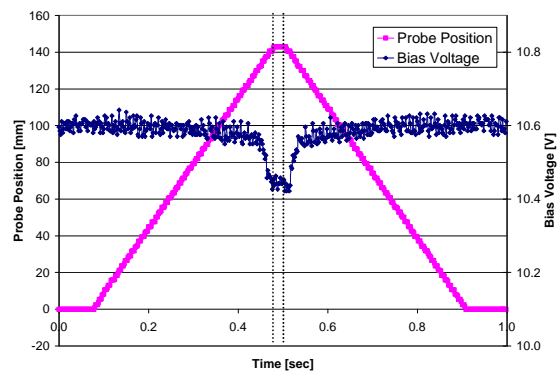


Fig. 10 – Sample bias voltage “sag” (10 V bias) without beam extraction. Dotted lines indicated dwell time at thruster and DCA centerline.

The voltage drop is thought to be a result of the changing “resistance” of the plasma as the probe is inserted into it combined with the use of a potentiometer to sweep through bias voltages. Figure 11 and the subsequent equations demonstrate that as  $R_{Plasma}$  changes during probe insertion,  $R_{eq}$  changes as well. The current flowing changes and the result is a change in the potential difference between the two electrodes. Minimizing this voltage fluctuation would require  $R_{Plasma} \ll R_2$ . This is not easily achieved without control over  $R_{Plasma}$  and the need to sweep  $R_2$  over a range of values to set our desired bias voltages. The voltage “sag” will be corrected for using the double probe circuit.

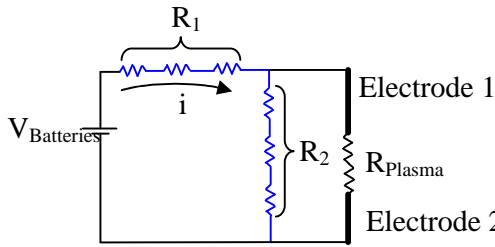


Fig 11 – Electrical diagram of bias voltage circuit ( $R_1$  and  $R_2$  are internal to potentiometer).

$$R_{eq} = R_1 + \left( \frac{1}{R_2} + \frac{1}{R_{Plasma}} \right)^{-1} \quad (2)$$

$$i = \frac{V_{Batteries}}{R_{eq}} \quad (3)$$

$$V_{Plasma} = V_{Batteries} - R_1 i \quad (4)$$

Figure 12 illustrates the data collection two dimensional matrix. From the oscilloscope raw data, the discharge current, probe collected current, and probe bias voltage can be calculated as a function of probe position. The resulting data were later reassembled to obtain the current-voltage characteristic of the double probe at each location in the radial sweep. Only data taken on the “in sweep” of the probe were used as “out sweep” data is more likely to be affected by the probe perturbation.

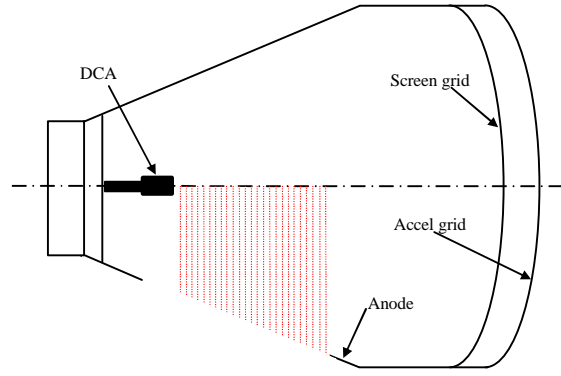


Fig. 12 – Data collection domain. The internal discharge mapping begins 2 mm downstream of the DCA face and extends to 39.69 mm (1.56 inches) in 25 steps giving axial resolution of 1.59 mm (1/16 of an inch).

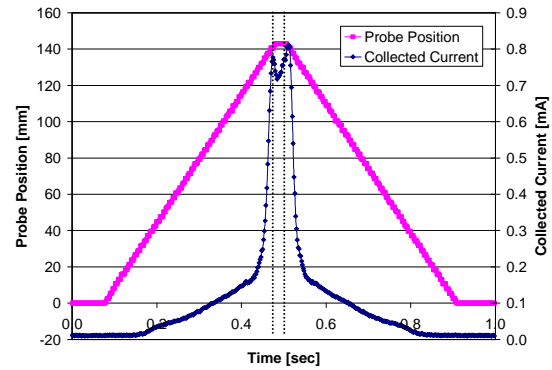


Fig. 13 – Representative radial sweep at 17.9 mm downstream of the DCA. DCA centerline (between dotted lines) is at 143 mm.

## Data Analysis

The scientific graphing package Igor was used to analyze the data. The data are read into Igor, which reassembles the data into individual characteristics at each position in the two-dimensional grid. The individual double probe characteristics were analyzed assuming an infinite, quasi-neutral, and quiescent plasma. The electron and ion mean free paths are much larger than the probe dimensions indicating a collisionless analysis. Particles are assumed to be collected without reflection or reaction inside the electrode collection area.

The presence of a magnetic field has a negligible effect on the probe measurements. The double probe analysis infers number density from the ion saturation current and therefore is unaffected by the reduction in electron saturation current caused by the presence of a magnetic field. The magnetic field can also lead to electron energy

distribution function (EEDF) anisotropy. Passoth<sup>18</sup> determined that EEDF anisotropy depended upon the ratio  $B/p_0$ , where  $p_0$  is the pressure in the containment vessel (in this case the discharge chamber). It has been shown experimentally that EEDF anisotropy was negligible for  $B/p_0 \leq 2.5 \times 10^6$  G/Torr.<sup>19</sup> In the FMT-2, B has a maximum (downstream of the DCA) of 107 G and the pressure in the discharge chamber is minimally estimated to be  $1 \times 10^{-4}$  Torr. The value of  $B/p_0$  for the worst case is  $1 \times 10^6$  therefore no substantial anisotropy in the EEDF is expected.

Each characteristic is fit with the theoretical hyperbolic tangent curve for a symmetric cylindrical double probe.<sup>11, 20, 21</sup>

$$I = I_{sat} \cdot \tanh\left(\frac{f}{2T_{ev}}\right) + A_1 \cdot f + A_2 \quad (5)$$

In Equation 5 the parameter  $A_1$  accounts for sheath expansion in the ion saturation region and  $A_2$  accounts for any offset current due to stray capacitance. Igor was used, incorporating the Levenberg-Marquardt method, to fit this equation to the experimental data.<sup>22</sup> Electron temperature can be determined immediately from the fit parameters. Using the Bohm<sup>11, 23, 24</sup> approximation for ion velocity the ion number density was calculated according to Equation 6.

$$n_i = \frac{I_{sat}}{A_s (qZ_i)^{3/2}} \sqrt{\frac{M_i}{T_{ev}}} \quad (6)$$

In this equation,  $A_s$  is initially considered to be the electrode surface area. The true collection area, which depends upon the thickness of the sheath surrounding the probe, is determined through an iterative process. Knowledge of the number density and electron temperature allow the Debye length to be calculated according to Equation 7.<sup>23, 24, 25</sup>

$$I_D = 743 \sqrt{\frac{T_{ev}}{n_e}} \quad (7)$$

Assuming quasi-neutrality  $n_e \approx n_i$  (in  $\text{cm}^{-3}$ ) readily gives  $\lambda_D$  (cm). The sheath thickness is of the order of the Debye length<sup>15</sup> and thus the ion collection area is now taken as a cylinder with a radius of the electrode radius plus one Debye length having the same length of the electrode. From this new collection area new plasma

parameters are calculated. The iterative process takes into account the slight departure from thin sheath assumption in the data analysis and continues until satisfactory convergence.

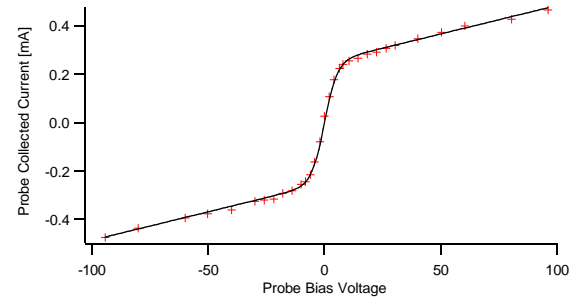


Fig. 14 – Plot of the data points taken for a typical characteristic curve (+) along with the hyperbolic tangent fit (–). Thirty-one bias voltage settings allowed for an adequate fit.

Because the number density is calculated from the ion saturation current and electron temperature calculation, errors in estimating the ion saturation current or the electron temperature are compounded in the calculation of the electron number density. Typical estimates for the error in electron temperature and electron number density are 20% and 50%, respectively.<sup>26</sup>

## Results and Discussion

For these initial experiments, radial sweeps were taken every 1.59 mm starting at a zero position 2 mm downstream of the DCA. A full set of data was taken for discharge conditions *without beam extraction* corresponding to Throttling Level 4. An incomplete data set was taken corresponding to Throttling Level 8. The test was unexpectedly shutdown when the double probe shield came loose covering the electrodes. Time constraints prohibited further testing.

Since the focus of this investigation is discharge cathode phenomena, the primary thruster operating conditions of concern are the discharge current and voltage. For each operating condition, the discharge current was set to the corresponding value in the NASA Throttling Conditions (TH Level) Tables. The main anode flow rate and discharge cathode flow rate were adjusted until the discharge voltage matched the respective values for the indicated NASA TH Level. The operating conditions of the FMT-2 are referred to as Discharge Conditions (DC Levels) instead of TH Levels. Below is an abbreviated list of telemetry focusing only upon the discharge parameters. For a complete listing

of thruster parameters see Table A.1 in the Appendix for DC Level parameters and NASA TH Level parameters, respectively.

Table 1 – Discharge conditions and reference NASA throttling parameters

Level	Vd	Jd	Main flow	Disch. cathode flow
	V	A	sccm	sccm
DC 4	25.4-25.8	6.05	8.1	2.29
TH 4	25.61	6.05	8.30	2.47

Figures 15 and 16 illustrate the calculated plasma parameters. The number densities fall within the expected range with values from  $1 \times 10^{10}$  -  $2 \times 10^{12}$   $\text{cm}^{-3}$  over the two dimensional grid investigated. As expected, the maximum number density occurs along the DCA centerline and falls off by at least an order of magnitude only 10 mm radially from the centerline axis. The measured number densities are well within the range required to cause DCA erosion from singly-ionized xenon that is consistent with the 8200 hour wear test results, as stipulated by Williams.<sup>2,6</sup> Williams' Langmuir probe data for a 6 A hollow cathode operating with an anode exhibit a similar drop off in number density with axial distance (along centerline) by an order of magnitude after 4 cm. In addition his maximum number density, occurring at the nearest location (5 mm) was calculated to be  $2 \times 10^{12}$   $\text{cm}^{-3}$ .<sup>6</sup> Williams electron temperature measurements increased with axial distance from 1.8 to 3.2 eV along centerline. Our reported off-axis maximum in electron temperature is not an expected result. Beattie and Matossian computed a spatially varying Maxwellian electron temperature profile whose maximum lies along the thruster centerline.<sup>12</sup> Although they studied a mercury ion thruster, one could draw the conclusion that while the electron temperature magnitudes may differ the overall trends should be similar. Their computation does not predict an increase in electron temperature with increasing axial distance from the keeper electrode as has been measured by other researchers.

Work done by Domonkos on hollow cathodes for a similar flowrate measure electron temperatures of 1.5 to 2.5 eV along centerline over the same axial range.<sup>13</sup> Again there is a general increase in electron temperature with increasing axial distance from the keeper electrode.

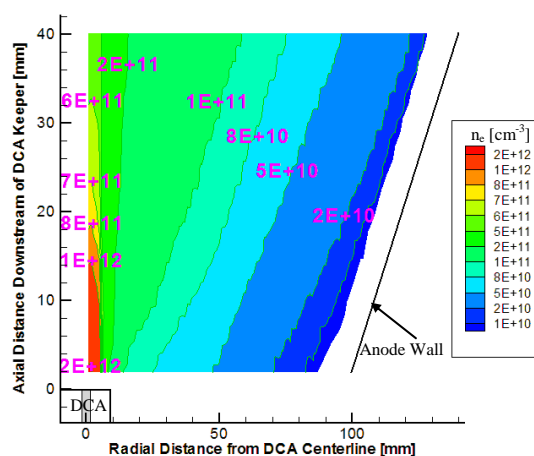


Fig. 15 – Electron number density calculations. Also shown are the DCA location and anode wall for reference.

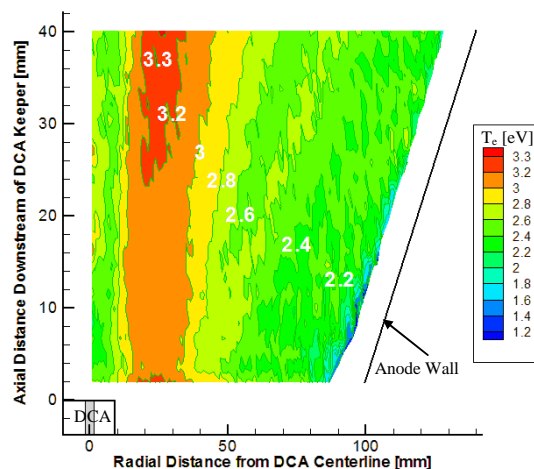


Fig. 16 – Electron temperature calculations. Also shown are the DCA location and anode wall for reference.

Foster and Patterson have taken high current hollow cathode measurements on an NSTAR type discharge chamber. Figure 17 illustrates the similar trends in number density measurements between double probe data taken in this investigation and those taken by Foster and Patterson.<sup>14</sup> The on-axis number densities agree remarkably well. In addition the two have similar profile shapes. The discrepancy between the two curves can easily be accounted for by the difference in discharge current and the error in electrostatic probe measurements.

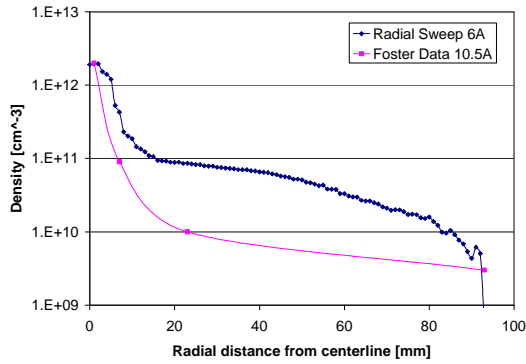


Fig. 17 – Number density comparison to Foster and Patterson data<sup>14</sup>. Both radial sets of data were taken 3 mm downstream of the DCA keeper exit plane.

### Error Discussion

Traditional estimates of the error in electrostatic probe measurements are typically 50% for electron number density and 20% for electron temperature.<sup>26</sup> While these errors are large, the relative error between two measurements using identical setups is not this high.

There are several different probe regimes that depend upon the fundamental lengths in the plasma. Care was taken to ensure that over the domain of interest, the probe radius is larger than the Debye length. This has been approximated as a thin sheath calculation and thus ion orbits are negligible when interpreting the probe characteristic.<sup>11, 15, 16</sup> The Debye length grows significantly as the radial distance from the discharge cathode is increased since the electron temperature is roughly constant while the electron number density falls off rapidly.

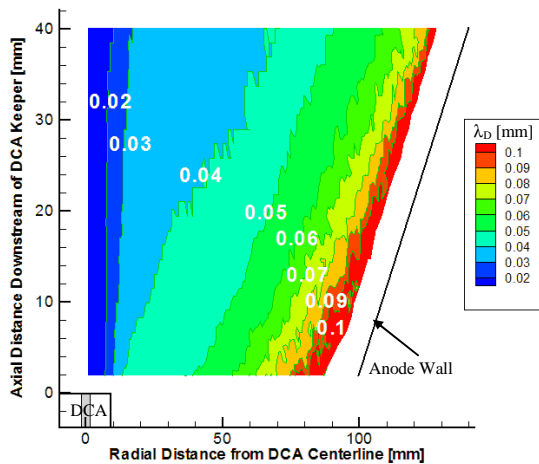


Fig. 18 – Debye length calculations. Also shown are the DCA location and anode wall for reference.

Under normal operation of a double probe, it is important that the electrode sheaths are not overlapping. Symmetric double probe theory assumes that the electrodes are identical and that they are close enough together that the plasma is identical at both positions. The current collected from one electrode is emitted by the other, however the two electrodes need to be “independent” from each other in that the plasma being measured is the only connection between the two. Overlapping of the electrode sheaths results in a means of “communication” between the two probes, which invalidates the double probe theory used. Estimating the sheath thickness, up to five times the Debye length, results in a maximum sheath thickness of roughly 0.5 mm, close to the anode wall, while the gap distance is 3.45 mm.

To ascertain the perturbation introduced by the probe, measurement of the discharge current is recommended. The need to measure the discharge current perturbation induced by the double probe has been taken care of by using a Hall Probe, in conjunction with an oscilloscope, to measure the discharge current as a function of position during each insertion of the double probe into the discharge chamber plasma. Below is a graph of the discharge current at discharge conditions corresponding to Throttle Level 4 *without beam extraction* during probe insertion.

We expect that the highest perturbation will be at the highest bias voltage setting, 100 V bias. Also we expect that the largest perturbation will occur for the sweeps closest to the discharge keeper face. We found that the discharge current perturbation was approximately 5% of the discharge current for this case. Indeed the discharge perturbation always remained less than 5% of the discharge current during probe insertion (for this thruster operating condition). Below is a representative graph of the typical discharge current perturbation as the probe is inserted into the discharge plasma.

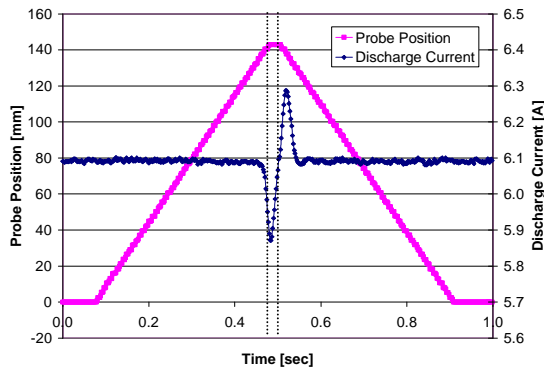


Fig. 19 – Sample discharge perturbation (10 V bias, 6.05 A, 24.5 – 24.8 V shown) *without beam extraction*. Dotted lines indicated dwell time at thruster and DCA centerline.

### Conclusions

A method of interrogating a two-dimensional grid inside the discharge chamber plasma has been demonstrated. A complete mapping of discharge plasma parameters was calculated for the thruster operating condition *without beam extraction*. The data were found to agree, in magnitude, with estimates for both electron temperature and number density. Electron number density profiles agree with similar measurements taken by Foster and Patterson.<sup>14</sup> The off-axis peak in electron temperature is an unexpected result which will require more testing to confirm and/or explain.

### Future Work

Future tests will take more double probe data over the two-dimensional grid downstream of the DCA. Three other operating conditions *without beam extraction* will be investigated to infer the effect of thruster operating condition on discharge plasma parameters. The double probe measurements will be taken over the same four operating conditions with beam extraction. After completing double probe measurements, an emissive probe will be employed to map the plasma potential inside the discharge chamber. This could validate or rule out the existence of a potential hill, which has been proposed as a possible explanation of DCA erosion.<sup>6</sup>

### Acknowledgements

We would like to thank Dr. George Williams and Dr. James Haas whose work at the University of Michigan has laid the foundation for this research. They have gone beyond the call of duty to offer direction, answer questions, and lend assistance.

We would like to thank the entire research group at PEPL who have been instrumental in this investigation.

We would also like to thank the NASA Glenn Research Center (GRC) for their financial support through research grant NAG3-2216 and for use of their equipment. We would especially like to acknowledge Dr. Matthew Domonkos (grant monitor), Dr. John Foster, and Dr. George Williams who have been the principal contacts at NASA GRC and offered assistance when called upon.

## References

- <sup>1</sup> <http://nmp.jpl.nasa.gov/ds1/gen/mission.html>
- <sup>2</sup> Polk, J. E., et al., "An Overview of the Results from an 8200 Hour Wear Test of the NSTAR Ion Thruster," AIAA Paper No. 99-2446, 35<sup>th</sup> AIAA / ASME / SAE / ASEE Joint Propulsion Conference, Los Angeles, CA, June 1999.
- <sup>3</sup> Williams, G. J., et al., "Characterization of FMT-2 Discharge Cathode Plume," IEPC Paper No. 99-104, 26<sup>th</sup> International Electric Propulsion Conference, Ketakiushu, Japan, Oct. 1999.
- <sup>4</sup> Anderson, J. R., et al., "Performance Characteristics of the NSTAR Ion Thruster During and On-Going Long Duration Ground Test," IEEE Paper No. 8.0303, IEEE Aerospace Conference, Big Sky, MT, Mar. 2000.
- <sup>5</sup> Domonkos, M. T., Foster, J. E., Patterson, M. J., "Investigation of Keeper Erosion in the NSTAR Ion Thruster," IEPC Paper No. 01-308, 27<sup>th</sup> International Electric Propulsion Conference, Pasadena, CA, Oct. 2001.
- <sup>6</sup> Williams, G. J., *The Use of Laser-Induced Fluorescence to Characterize Discharge Cathode Erosion in a 30 cm Ring-Cusp Ion Thruster*, Ph.D. Dissertation, University of Michigan, 2000.
- <sup>7</sup> Walker, M. L. R., Gallimore, A. D., "Pressure Map of a Facility as a Function of Flow Rate to Study Facility Effects," AIAA-2002-3815, 38<sup>th</sup> Joint Propulsion Conference, Indianapolis, Indiana, July 7-10, 2002.
- <sup>8</sup> Hofer, R. R., Peterson, P. Y., Gallimore, A. D., "Characterizing Vacuum Facility Backpressure Effects on the Performance of a Hall Thruster," IEPC Paper No. 01-045, 27<sup>th</sup> International Electric Propulsion Conference, Pasadena, CA, Oct. 2001.
- <sup>9</sup> Dushman, S., *Scientific Foundations of Vacuum Technique*, Vol. 4, Wiley, New York, 1958.
- <sup>10</sup> Haas, J. W., et al., "Development of a High-Speed, Reciprocating Electrostatic Probe System for Hall Thruster Interrogation," *Review of Scientific Instruments*. Vol. 71, No. 11, pp. 4131-4138, Nov. 2000.
- <sup>11</sup> Mott-Smith, H., and Langmuir, I. *Physics Review*, Vol. 28, 727, 1926.
- <sup>12</sup> Beattie, J. R., and Matossian, J. N., *Mercury Ion Thruster Technology Final Report*, NASA CR-174974, Hughes Research Labs. Feb. 1983 – Oct. 1984.
- <sup>13</sup> Domonkos, M. T., *Evaluation of Low-Current Orificed Hollow Cathode*, Ph.D. Dissertation, University of Michigan, 1999.
- <sup>14</sup> Foster, J. E., and Patterson, M. J., "Plasma Emission Characteristics from a High Current Hollow Cathode in an Ion Thruster Discharge Chamber," AIAA-2002-4102, 38<sup>th</sup> Joint Propulsion Conference, Indianapolis, Indiana, July 7-10, 2002.
- <sup>15</sup> Hershkowitz, N., "How Langmuir Probes Work," *Plasma Diagnostics*. Nuclear Engineering and Engineering Physics Department, University of Wisconsin-Madison, 1989.
- <sup>16</sup> Schott, L. *Plasma Diagnostics: Ch. 11 Electrical Probes*, Edited by Lochte-Holtgreven, American Elsevier Publishing Co, New York, N.Y., 1968.
- <sup>17</sup> Haas, J. W., *Low-Perturbation Interrogation of the Internal and Near-Field Plasma Structure of a Hall Thruster using a High-Speed Probe Positioning System*, Ph.D. Dissertation, University of Michigan, 2001.
- <sup>18</sup> Passoth, E., et al., "An experimental study of plasma density determination by a cylindrical Langmuir probe at different pressures and magnetic fields in a cylindrical magnetron discharge in heavy rare gases," *Journal of Physics D*, Vol. 30, No. 12, June 1997, p. 1763-77.
- <sup>19</sup> Aikawa, H., "The Measurement of the Anisotropy of Electron Distribution Function of a Magnetized Plasma," *Journal of the Physical Society of Japan*, Vol. 40, No. 6, June 1976.
- <sup>20</sup> Johnson, E. O., and Malter, L., "A Floating Double Probe Method for Measurements in Gas Discharges," *Physics Review*, Vol. 80, No. 1, pp. 58 - 68, Oct., 1950.
- <sup>21</sup> Boedo, et al, "Fast Scanning Probe for Tokamak Plasmas," *Review of Scientific Instruments*, Vol. 69, No. 7, pp. 2663-2670, July, 1998.
- <sup>22</sup> Smith, B. A, and Overzet, L., J., "Improvements to the Floating Double Probe for Time-resolved Measurements in Pulsed RF Plasmas," *Review of Scientific Instruments*, Vol. 69, No. 3, pp. 1372 – 1377, March, 1998.
- <sup>23</sup> Chen, F.F. *Introduction to Plasma Physics and Controlled Fusion: Vol. 1 Plasma Physics*, Plenum Press, New York, N.Y., 1984.

<sup>24</sup> Chen, F. F., *Plasma Diagnostic Techniques: Ch. 4 Electric Probes*, Edited by Huddleston and Leonard, Academic Press, New York, N.Y., 1965.

<sup>25</sup> *NRL Plasma Formulary*, NRL/PU/6790--00-426, Naval Research Laboratory, Washington, D.C., 2000.

<sup>26</sup> Hutchinson, I. H., *Principles of Plasma Diagnostics*, Cambridge University Press, New York, N.Y., 1987

## Appendix

Table A.1 – Full thruster telemetry for Discharge Conditions for plasma parameter measurement without beam extraction. Also listed is the NASA throttling table telemetry for comparison.

	V <sub>b</sub>	J <sub>b</sub>	V <sub>a</sub>	J <sub>a</sub>	V <sub>d</sub>	J <sub>d</sub>	V <sub>nk</sub>	J <sub>nk</sub>	Main flow	Disch. cathode flow	Neutralizer cathode flow	V <sub>ck-cc</sub>	Pressure
Level	V	A	V	mA	V	A	V	A	sccm	sccm	sccm	V	Torr
DC 4	-	-	-	-	25.4 -25.8	6.05	18.00	2.0	8.1	2.29	-	9.5-9.9	1.6E-06
TH 4	1100	0.71	-150	1.93	25.61	6.05	16.26	2.0	8.3	2.47	2.40	-	-